Deformation-driven diffusion and plastic flow in amorphous granular pillars

Wenbin Li,[1] Jennifer M. Rieser,[2] Andrea J. Liu,[2] Douglas J. Durian,[2,*] and Ju Li[1,3,†]

[1]*Department of Materials Science and Engineering, Massachusetts Institute of Technology, Cambridge, Massachusetts 02139, USA*
[2]*Department of Physics and Astronomy, University of Pennsylvania, Philadelphia, Pennsylvania 19104, USA*
[3]*Department of Nuclear Science and Engineering, Massachusetts Institute of Technology, Cambridge, Massachusetts 02139, USA*

We report a combined experimental and simulation study of deformation-induced diffusion in compacted quasi-two-dimensional amorphous granular pillars, in which thermal fluctuations play a negligible role. The pillars, consisting of bidisperse cylindrical acetal plastic particles standing upright on a substrate, are deformed uniaxially and quasistatically by a rigid bar moving at a constant speed. The plastic flow and particle rearrangements in the pillars are characterized by computing the best-fit affine transformation strain and nonaffine displacement associated with each particle between two stages of deformation. The nonaffine displacement exhibits exponential crossover from ballistic to diffusive behavior with respect to the cumulative deviatoric strain, indicating that in athermal granular packings, the cumulative deviatoric strain plays the role of time in thermal systems and drives effective particle diffusion. We further study the size-dependent deformation of the granular pillars by simulation, and find that different-sized pillars follow self-similar shape evolution during deformation. In addition, the yield stress of the pillars increases linearly with pillar size. Formation of transient shear lines in the pillars during deformation becomes more evident as pillar size increases. The width of these elementary shear bands is about twice the diameter of a particle, and does not vary with pillar size.

PACS number(s): 45.70.−n, 47.57.Gc, 83.50.−v, 83.80.Fg

I. INTRODUCTION

Disordered materials such as metallic glasses can exhibit highly localized deformation and shear band formation [1,2]. Most experiments on these systems, however, use loading geometries in which there are free boundaries and inhomogeneous strains, while simulations have typically focused on systems with periodic boundary conditions under homogeneously applied shear strain. To understand at a microscopic level the effects of loading geometry on the macroscopic mechanical response, it is useful to study a disordered system in which individual particles can be imaged and tracked as they rearrange under an applied load. Here we introduce a granular packing—a packing of discrete macroscopic particles for which thermal agitation plays a negligible role [3,4]—in a pillar geometry commonly used for mechanical testing of metallic glasses. Cubuk and Schoenholz *et al.* showed that machine learning methods can be used to identify a population of grains that are likely to rearrange in these two-dimensional (2D) pillars [5]. In this paper, we combine experiment and simulation to study the response of the pillars to athermal, quasistatic, uniaxial compression.

One question of interest is how the mechanical response of the pillar depends on pillar size. We find that the pillar shape evolves under load in a self-similar fashion, so that the shape of the pillar at a given strain is independent of system size. We also find that as the pillars deform, the strain rate localizes into transient lines of slip, whose thickness of a few particle diameters is independent of system size. Thus, the system is self-similar in shape at the macroscopic scale, but, surprisingly, its yielding is not self-similar at the microscopic scale.

A second question concerns the random motions of particles as they rearrange under inhomogeneous loading conditions. Because particles jostle each other, they display diffusive behavior in homogeneously sheared systems that are devoid of random thermal fluctuations [6]. Recently, crystal nucleation and growth were observed *in situ* in mechanically fatigued metallic glasses at low temperature [7]. Crystallization is typically thought to require diffusion. Therefore, it was suggested that the "shear transformation zones" (STZs) [2] should be generalized to "shear diffusion transformation zones" (SDTZs) [7,8], to reflect the contributions of random motions driven by loading, even under inhomogeneous conditions. Our amorphous granular pillar is an athermal system as far as the macroscopic particles are concerned (effective vibrational temperature ≈0), so our experiment and simulations can examine how inhomogeneous loading affects particle motion. We find that the idea of load-induced diffusion can be generalized to inhomogeneous loading by replacing time with the cumulative deviatoric strain, and the mean-squared displacement with the mean-squared displacement of a particle relative to the best-fit affine displacement of its neighborhood (i.e., the mean-squared nonaffine displacement [9]). With this generalization, we observe that the mean-squared nonaffine particle displacement crosses over from ballistic to diffusive behavior as a function of the cumulative deviatoric strain.

The article is organized as follows. In Sec. II, we describe the experimental and simulation setup, as well as the simulation methodology, of 2D amorphous granular pillars under uniaxial and quasistatic deformation. Section III describes the results of our combined experiments and simulations on the deformation of a 2D granular pillar containing 1000 particles. In Sec. IV, we discuss the exponential crossover of nonaffine particle displacement from ballistic to diffusion with respect to cumulative deviatoric strain. Section V presents our simulation results on the size-dependent deformation of large 2D granular pillars. Then we conclude the article in Sec. VI.

_____
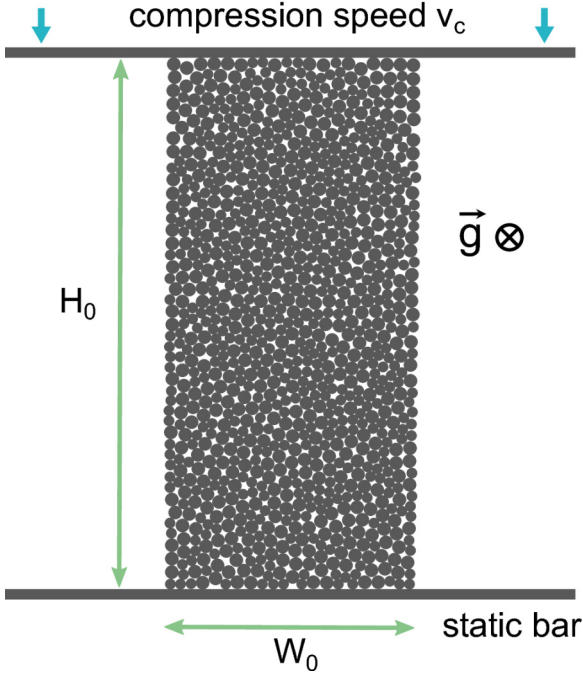*djdurian@physics.upenn.edu
†liju@mit.edu

FIG. 1. (Color online) Top view of the experimental/simulation setup. A two-dimensional pillar of granular particles on a frictional substrate is deformed quasistatically and uniaxially by a rigid bar from one side. The direction of gravity is perpendicular to the substrate. The compacted, disordered granular packing consists of a 50%-50% mixture of bidisperse cylindrical-shape grains. The ratio of radius between large and small grains is 4:3. The aspect ratio of the pillar, defined as the initial height of the pillar (H_0) divided by the initial width (W_0), is 2:1. The pillar is confined between two rigid bars placed at the top and bottom end of the pillar. The top bar deforms the pillar with a constant speed v_c while the bottom bar is kept static.

II. METHODS

The compacted 2D amorphous granular pillars in our study consist of a 50%-50% mixture of bidisperse cylindrical particles (grains) standing upright on a substrate. A top view of the schematic setup is shown in Fig. 1. The pillars have aspect ratio $H_0/W_0 \approx 2$, where H_0 and W_0 are the original height and width of the pillars, respectively. In our experiment, the cylindrical granular particles are made of acetal plastic. The diameter of the large grains in the pillars, denoted by D, is 1/4 inch (0.635 cm), while for the small grains the diameter d has the value of 3/16 inch (0.476 25 cm). The ratio of diameter between large and small grains is therefore $D/d = 4/3$. Both types of grains are 3/4 inch (1.905 cm) tall. The masses for the large and small grains are 0.80 g and 0.45 g, respectively. The pillars are confined between a pair of parallel bars. The bottom bar is static while the top bar deforms the pillars uniaxially with a slow, constant speed $v_c = 1/300$ inch per second (0.008 466 7 cm/sec). The force sensors connected to the bars measure the forces on the top and the bottom bars, and the trajectory of each particle in a pillar is tracked by a high-speed camera mounted above the pillar. The basic parameters in our simulation, including the size and mass of the grains, as well as the velocity of the bars, are the same as in

the experiment. Further experimental details will be described in an upcoming paper [10,11].

A. Packing generation protocol

Properly prepared initial configurations are crucial for the study of the mechanical properties of amorphous solids. In our experiment, a 50%-50% random mixture of bidisperse grains is compacted to form a pillar with aspect ratio 2 to 1. To facilitate direct comparison between experiment and simulation, for small-sized pillars (number of grains in the pillar $N = 1000$), the simulation initial conditions are taken from the experimental data, which were then relaxed in simulation to eliminate particle overlapping that results from measurement error. For large-sized pillars, which can only be studied by simulation, we generate compacted, amorphous granular pillars through computer simulation, using the protocol described below. The particle area density in the simulation-generated pillar is controlled to be at the onset of jamming transition [12]. To generate the initial conditions, we assign the following truncated Lennard-Jones potential with purely repulsive interaction to the large (L) and small (S) grains,

$$U_{\alpha\beta}(r) = \begin{cases} \epsilon[(\sigma_{\alpha\beta}/r)^{12} - 2(\sigma_{\alpha\beta}/r)^6] & \text{for } r < \sigma_{\alpha\beta}, \\ -\epsilon & \text{for } r \geqslant \sigma_{\alpha\beta}, \end{cases} \quad (1)$$

where the subscripts α, β denote L or S. The zero-force cutoff distances $\sigma_{\alpha\beta}$ are chosen to be the sum of radii of two particles in contact, namely $\sigma_{LL} = D$, $\sigma_{LS} = 7D/8$, and $\sigma_{SS} = 3D/4$, where D is the diameter of a large grain. We note that this potential will only be used to generate the initial conditions of the granular packings, and is different from the particle interaction model we describe later for the deformation of the granular pillars.

To create a disordered granular packing with 50%-50% mixture of N total number of large and small grains, a rectangular simulation box with dimensions $\Lambda \times 2\Lambda$ is initially created, where the width of the box Λ is chosen such that the initial particle area density, $\rho = N/2\Lambda^2$, is slightly above the particle overlapping threshold. We then randomly assign the positions of the particle within the simulation box, and subsequently use the conjugate-gradient (CG) method to minimize the total potential energy of the system. Periodic boundary conditions are applied during this process. The particle positions are adjusted iteratively until the relative change of energy per particle between two successive CG steps is smaller than 10^{-12}. When this stage is reached, the pressure of the system is calculated using the following virial formula:

$$p = -\frac{1}{2A} \sum_{i>j} r_{ij} \frac{dU}{dr_{ij}}, \quad (2)$$

where A is the area of the simulation box and r_{ij} is the distance between particles i and j. If the pressure is greater than zero, both dimensions of the simulation box will be enlarged by a fraction of 10^{-5}, and the particles in the box will be mapped to the corresponding new positions in the enlarged box via affine transformation. CG energy minimization will then be carried out on the new configuration. This iterative process stops when the calculated pressure of the system at the end
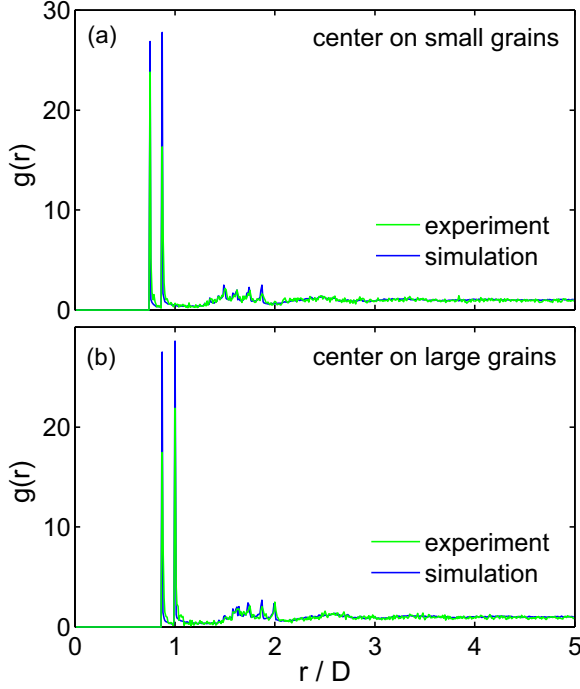
FIG. 2. (Color online) Comparison of the radial distribution functions $g(r)$ for experiment-derived and simulation-generated initial conditions computed using (a) small grains as the central particles and (b) larger grains as the central particles are shown respectively. The distance r is scaled by the diameter D of the large particles.

of a CG run becomes smaller than $10^{-10}\epsilon/D^2$. The final configuration will be taken as the initial conditions of close-packed 2D amorphous granular assembly. Free boundaries are then implemented on the lateral sides of simulation box to create a pillar with 2:1 aspect ratio. Calculation of radial distribution functions for different-sized pillars indicates that the structure of the amorphous assemblies generated following the above procedures does not show noticeable size dependence. Comparison of the radial distribution functions computed for the experimental and simulation-generated initial conditions is shown in Fig. 2.

B. Simulation methodology

We use molecular dynamics (MD) to simulate the quasistatic deformation of the 2D granular pillars. The simulation force model includes three components: the grain-grain interaction, the grain-bar interaction, and the grain-substrate interaction. Each of these forces will be described in the remainder of this subsection.

1. Grain-grain interaction

As illustrated in Fig. 3(a), the interaction between two grains includes normal and tangential contact force, which are denoted by $\mathbf{F}_n$ and $\mathbf{F}_t$, respectively. Two grains experience a repulsive normal contact force if the distance between the particle centers is smaller than the sum of their radii. For two smooth, elastic cylindrical particles with parallel axes, the normal contact force as determined by the Hertzian theory
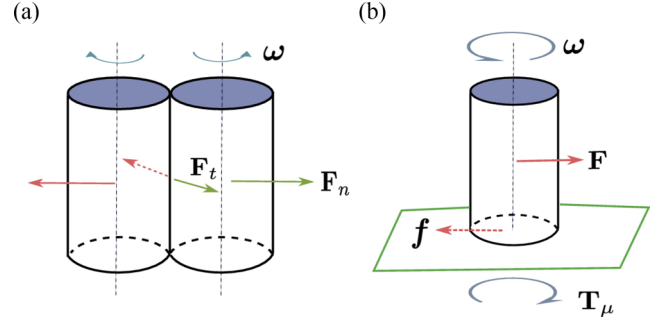

FIG. 3. (Color online) (a) Illustrations of grain-grain interaction in the granular pillar. The contact force between two grains consists of normal repulsive contact force $\mathbf{F}_n$ and tangential shear contact force $\mathbf{F}_t$. (b) Illustration of grain-substrate interaction. If the velocity of a grain i is nonzero, or the vector sum of the forces on the grain due to other grains and the bars is nonzero, the substrate will exert a frictional force $\mathbf{f}$ on the grain, the maximum value of which is $m_i g \mu$, where m_i is the mass of the particle, g is the gravity acceleration constant, and μ denotes the friction coefficient between the grain and the substrate. Likewise, if the angular velocity of the grain is nonzero or the torque on the grain due to other interactions is nonzero, the substrate will induce a frictional torque whose maximum magnitude is $|\mathbf{T}_{\mu,i}| = \frac{2}{3} m_i g \mu R_i$, where R_i is the radius of the particle.

of contact mechanics is proportional to the indentation depth between the two particles [13]. For our granular particles, denote by $\mathbf{r}_i$ and $\mathbf{r}_j$ the positions of particles i and j, and denote by $\mathbf{r}_{ij} = \mathbf{r}_i - \mathbf{r}_j$ the distance vector between the two particles; the indentation depth δ_{ij} is calculated as

$$\delta_{ij} = R_i + R_j - r_{ij}, \tag{3}$$

where $r_{ij} = |\mathbf{r}_{ij}|$. R_i and R_j are the radii of particles i and j. δ_{ij} will be zero if the two particles are not in contact. The normal contact force acting on the particle i by particle j is then given by

$$\mathbf{F}_{n_{ij}} = k_n \delta_{ij} \mathbf{n}_{ij}, \tag{4}$$

where $\mathbf{n}_{ij} = \mathbf{r}_{ij}/r_{ij}$, and k_n is the normal contact stiffness. The corresponding normal contact force on particle j is given by Newton's third law, namely, $\mathbf{F}_{n_{ji}} = -\mathbf{F}_{n_{ij}}$. In Hertzian theory of contact mechanics [13], the constant k_n for two cylinders in contact can be calculated as

$$k_n = \frac{\pi}{4} E^* l, \tag{5}$$

where l is the height of the cylinders. E^* is the normalized contact elastic modulus, which is computed from the respective elastic modulus of the two cylinders, E_1 and E_2, and their Poisson's ratios, ν_1 and ν_2:

$$\frac{1}{E^*} = \frac{1 - \nu_1^2}{E_1} + \frac{1 - \nu_2^2}{E_2}. \tag{6}$$

The existence of a friction force between two particles in contact is a characteristic feature of granular materials. Appropriate modeling of contact friction is crucial to the study of granular dynamics. The tangential frictional force between two grains in contact can be very complicated in reality [14]. We adopt the history-dependent shear contact model initially developed by Cundall and Strack [15]. This well-tested model

has been used by many others to model the dynamics of granular assemblies [14,16–24]. The essence of this model is to keep track of the elastic shear displacement of two particles throughout the lifetime of their contact, and applying the Coulomb elastic yield criterion when the displacement reaches a critical value. Our implementation of the Cundall-Strack model follows Silbert *et al.* [14]. Specifically, the tangential contact force between particle i and j is calculated as

$$\mathbf{F}_{t_{ij}} = -k_t \mathbf{u}_{t_{ij}}, \tag{7}$$

where the shear displacement $\mathbf{u}_{t_{ij}}$ is obtained by integrating the tangential relative velocities of the two particles during the lifetime of their contact [14]. Here k_t is the tangential contact elastic modulus. It is taken to be proportional to the normal contact stiffness k_n. Following Silbert *et al.*, we choose $k_t = \frac{2}{7}k_n$. Previous studies have shown that the dynamics of system is relatively insensitive to this parameter [14], which is confirmed by our own simulation.

To model the elastic yield of shear contact, the magnitude of $\mathbf{u}_{t_{ij}}$ is truncated to satisfy the Coulomb yield criterion $|\mathbf{F}_{t_{ij}}| \leqslant |\mu_g \mathbf{F}_{n_{ij}}|$, where μ_g is the friction coefficient between the grains.

The tangential contact force will induce torques on the two grains in contact, as given by

$$\mathbf{T}_{ij} = -R_i \hat{\mathbf{n}}_{ij} \times \mathbf{F}_{t_{ij}}. \tag{8}$$

Here $\mathbf{T}_{ij}$ is the torque exerted by grain j on grain i due to the tangential contact force $\mathbf{F}_{t_{ij}}$.

2. Grain-bar interaction

The grain-bar interaction is modeled in a similar way to the grain-grain interaction. The bar is essentially treated as a rigid grain with infinitely large radius. When a grain comes in contact with a bar, the grain can experience normal and shear contact force induced by the bar, and the shear contact force is also calculated by tracking the elastic shear displacement between the grain and the bar. The motion of the moving bar is not affected by the grains. The static bar at the bottom side of the pillar is always static, while the top bar deforms the pillar at a constant speed v_c. Compared to grain-grain interaction, the interaction parameters between the grains and the bar is slightly modified. The bars are modeled as rigid, undeformable bodies with infinite elastic modulus. Consequently, the effective interaction modulus E^* between the bars and the grains, based on Eq. (6), is twice as large as that between the grains. Therefore, from Eq. (5), the normal interaction stiffness between the bars and the grains is twice as large as that between the grains, i.e., k_n(grain-bar) = $2k_n$(grain-grain). Since the shear modulus of contact k_t is proportional to k_n, we have k_t(grain-bar) = $2k_t$(grain-grain) as well.

3. Grain-substrate interaction

The substrate can induce both frictional force and torque on the grains, as illustrated in Fig. 3(b). If a grain is initially static, unless the magnitude of total force due to other grains/bars is larger than the maximum frictional force that can be exerted by the substrate $|\mathbf{f}_i| = m_i g \mu$, the substrate frictional force will cancel out other forces on the grain and the particle

will continue to have zero velocity. Here m_i is the mass of the grain i, g is the gravitational acceleration, and μ denotes the frictional coefficient between the grains and the substrate. In another case, if the velocity of the grain is nonzero, the substrate will induce a frictional force opposite to the direction of particle motion, with magnitude $|\mathbf{f}_i| = m_i g \mu$. A similar algorithm applies to the rotational motion of a particle. An initially static grain will not start to rotate unless the torque due to other interactions surpasses the maximum substrate-induced frictional torque $|\mathbf{T}_{\mu_i}| = \frac{2}{3}m_i g \mu R_i$, where R_i is the radius of the cylindrical-shape particle. The prefactor $\frac{2}{3}$ is based on the assumption that frictional force is evenly distributed on the circular contact interface between a cylindrical-shape grain and the substrate. If the angular velocity of the grain is nonzero, a frictional torque

$$\mathbf{T}_{\mu,i} = -\frac{2}{3}m_i g \mu R_i \hat{\boldsymbol{\omega}}_i \tag{9}$$

will slow down the rotational motion of the particles, where $\hat{\boldsymbol{\omega}}_i = \boldsymbol{\omega}_i/|\boldsymbol{\omega}_i|$ and $\boldsymbol{\omega}_i$ denotes the angular velocity of particle i.

4. Equations of motion

Total forces and torques on each grain, determined by summing contributions discussed in Secs. II B 1–II B 3, are used to update the velocities of the grains according to Newtonian equations of motion:

$$m_i \frac{d^2 \mathbf{r}_i}{dt^2} = \mathbf{F}_i, \quad I_i \frac{d\boldsymbol{\omega}_i}{dt} = \mathbf{T}_i, \tag{10}$$

where $\mathbf{F}_i$ and $\mathbf{T}_i$ are the total force and torque on the particle i respectively. $I_i = \frac{1}{2}m_i R_i^2$ is the moment of inertia for grain i. The standard velocity Verlet integrator is used to update the positions and velocities of the particles, while a finite difference method is used to integrate the first-order differential equation for the angular velocities.

There is a subtle numerical issue that must be addressed when modeling velocity and angular velocity changes of the particles in the presence of the damping effects of a frictional substrate. In numerical integration of equation of motion, time is discretized into small time steps with each time step being a small increment δt. To complete the simulation within a reasonable time frame, δt cannot be too small, which means that the changes of velocity and angular velocity of the grains due to the substrate-induced force and torque within a time step are not infinitesimal. Hence, the motion of particles might not be able to be brought to a halt by the substrate; the velocity and angular velocity of the particles could oscillate around zero. Consider, for example, a stand-alone cylindrical grain with initial velocity $\mathbf{v}_i$ and angular velocity $\boldsymbol{\omega}_i$. Without other interactions, the substrate will induce friction $|\mathbf{f}_i| = m_i g \mu$ and frictional torque $|\mathbf{T}_{\mu,i}| = 2m_i g \mu/3$ on the grain, which slows down both the translational and rotational motion of the grain. According to the equations of motion in Eq. (10), the translational and rotational acceleration will be $a_v = g\mu$ and $a_\omega = 4g\mu/(3R_i)$, with R_i being the radius of particle i. Hence, within a time step δt, the change of velocity or angular velocity is a finite number: $\delta v = g\mu\delta t$, $\delta\omega = 4g\mu\delta t/(3R_i)$. If the velocity or angular velocity have been damped to values below these two numbers, they cannot be damped further but instead oscillate around zero, which is clearly a numerical

artifact. To work around this issue, we introduce two small parameters

$$\xi_v = g\mu\delta t, \quad \xi_{\omega_i} = \frac{4g\mu}{3R_i}\delta t, \tag{11}$$

such that when $|\mathbf{v}_i| < \xi_v$ and $|\sum_j \mathbf{F}_{ij} + \mathbf{F}_i^{\text{bar}}| \leqslant m_i g\mu$ are both satisfied, the velocity and total force on the particle will be set to zero. Here $\mathbf{F}_{ij}$ is the force of particle j on particle i, and $\mathbf{F}_i^{\text{bar}}$ is the force of the bars on particle i. Similarly, for the rotational motion, if $|\boldsymbol{\omega}_i| < \xi_{\omega_i}$ and $|\sum_j \mathbf{T}_{ij} + \mathbf{T}_i^{\text{bar}}| \leqslant \frac{2}{3}m_i g\mu R_i$, the angular velocity and total torque of the particle are set to zero.

C. Choice of simulation model parameters

The independent parameters in the interaction model of our simulation include the grain-grain stiffness k_n, grain-grain friction coefficient μ_g, grain-substrate friction coefficient μ, and the time step for integration of equations of motion δt. Among these parameters, μ has been experimentally measured to be around 0.23. Hence $\mu = 0.23$ will be adopted in our simulations. The grain-grain friction coefficient μ_g is unknown. We have carried out simulation using multiple values of μ_g, and the results indicate that choosing $\mu_g = 0.2$ achieves reasonable agreement between the experiment and simulation. Due to the quasistatic nature of the pillar deformation, the incremental force on a grain by the bar within one time step δt must be much smaller than the maximum static friction by the substrate on a grain, namely

$$2k_n v_c \delta t \ll m_i g\mu, \tag{12}$$

where v_c is the speed of the top moving bar. Hence, the smaller the value of δt, the higher the value of k_n that can be explored in simulation. While there is no physical reason for a lower bound of δt, smaller δt results in an increased time span to complete simulation. Realistic consideration leads to our choice of $\delta t = 10^{-5}$ s. The upper bound of allowed k_n calculated from Eq. (12) is considered to be smaller than the real contact stiffness of two particles in experiment. For this reason, we have systematically studied the influence of k_n on the simulation results in a small-sized pillar containing 1000 grains. The relatively small sized pillar allows us to use $\delta t = 10^{-6}$ s and thus access a wider range of k_n, from $k_n = 1$ N/mm to $k_n = 100$ N/mm. The results indicate that the statistical behaviors of deformation dynamics, such as flow stress and particle-level deformation characteristics, are not significantly influenced by the value of the k_n. We therefore choose $k_n = 10$ N/mm and $\delta t = 10^{-5}$ s in our simulation.

The results of our study will be expressed in terms of several characteristic units. Length will be expressed in the diameter of the large grains D or the radius $R = D/2$. The unit of velocity will be the bar speed v_c and the unit of time will be R/v_c, which is the time it takes for top bar to move over a distance equal to R. The units for force and stress will be $mg\mu$, $mg\mu/D$, respectively, where for convenience, we will use the symbol m to denote the mass of a large grain. $mg\mu$ is thus the minimum force to induce the translational motion of a stand-alone large grain and $mg\mu/D$ is the corresponding averaged stress of the bar on the grain.
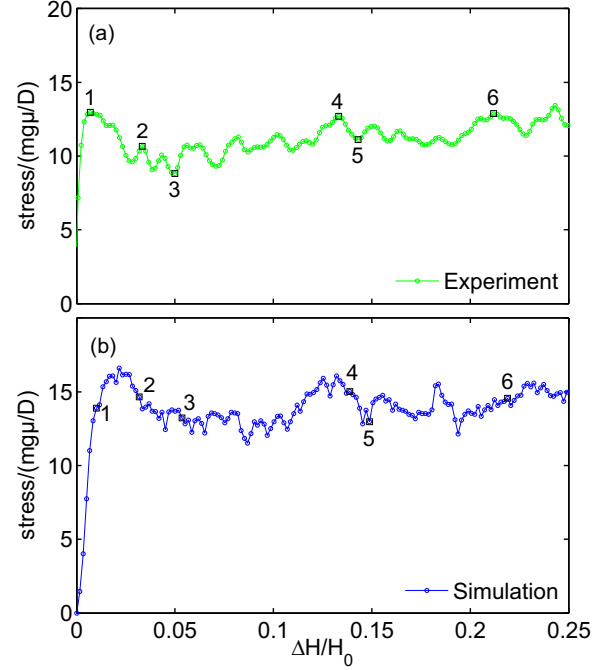

FIG. 4. (Color online) Comparison between the (a) experimental and (b) simulation stress-strain curves for the deformation of a $N = 1000$ granular pillar. The compressing stress is measured in units of $mg\mu/D$, while the strain is computed as the change of pillar height (ΔH) divided by the original height of the pillar H_0. The numerical labels (1–6) indicate the stress strain values at which deformation characteristics in the pillar will be compared side-by-side between experiment and simulation.

III. COMBINED EXPERIMENT AND SIMULATION ON DEFORMATION OF SMALL-SIZED PILLARS

Deformation of an $N = 1000$ pillar has been studied by both experiment and simulation. The experimental initial particle arrangement in the pillar is the same as those depicted in Fig. 1. To facilitate comparison between experiment and simulation, our parallel simulation of pillar deformation uses the experimentally measured initial conditions. In the simulation, the initial conditions are then relaxed via energy minimization to eliminate particle overlap resulting from measurement uncertainty. When the pillar is deformed by the moving bar, the strain of deformation ε is defined as the change of pillar height ΔH divided by the original height of the pillar H_0, namely, $\varepsilon \equiv \Delta H/H_0$. The deformation stress σ is calculated as the normal force on the top moving bar F_{bar} divided by the maximum width of the pillar near the top edge W, namely $\sigma \equiv F_{\text{bar}}/W$.

Figure 4 shows the experimental and simulation stress-strain curve of the $N = 1000$ pillar. The measured stress shows yielding behavior when the deformation strain exceeds a very small value ε_y. From our simulation, we find that the yield strain ε_y in general becomes smaller as the grain-grain stiffness k_n or the packing density of the pillar is increased. The yield stress σ_y however shows little dependence on k_n. The parameter that affects σ_y most is found to be the grain-grain friction coefficient μ_g. In the range of μ_g we have studied (μ_g from 0 to 0.3), σ_y increases monotonically with the increase
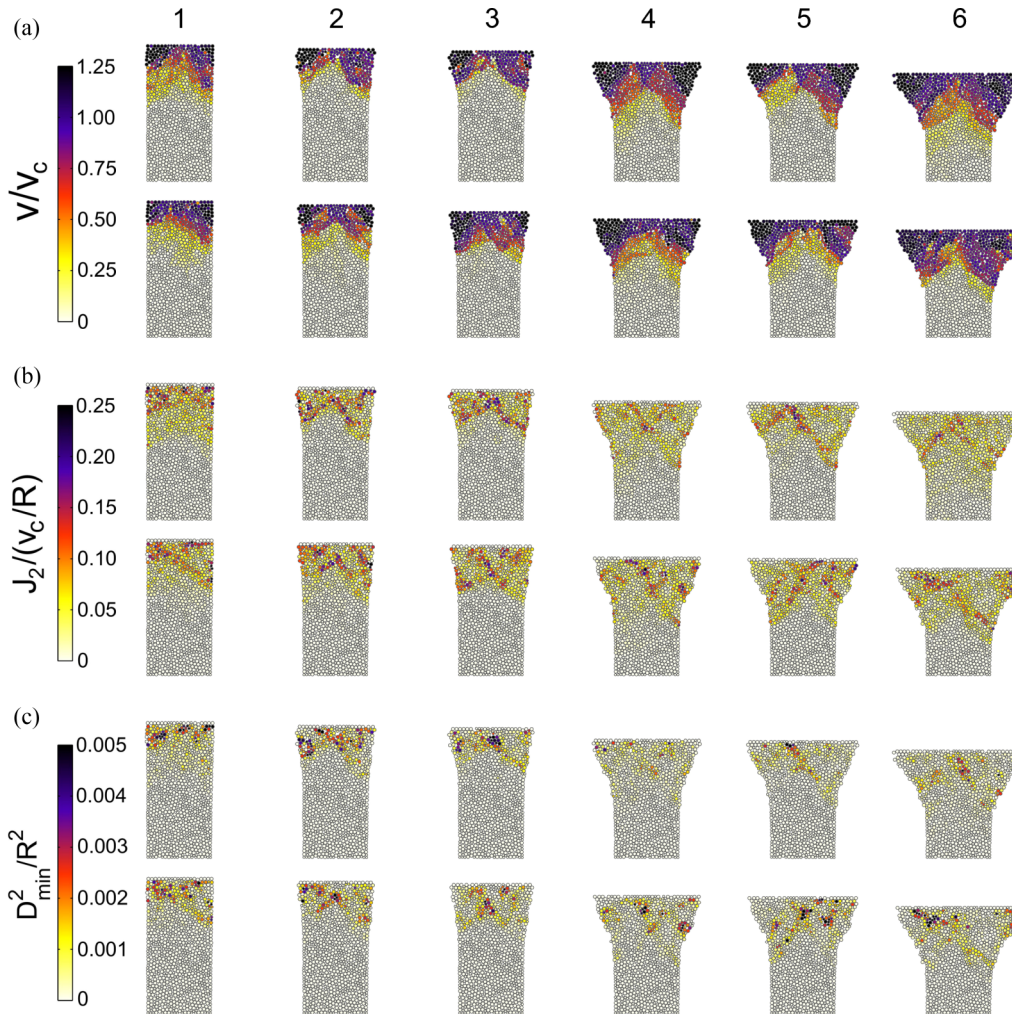
FIG. 5. (Color online) Comparison between experiment and simulation of the particle velocity v, deviatoric strain rate J_2, and nonaffine displacement $D_{\min}^2$ during deformation of a $N = 1000$ granular pillar. The six stages of deformation (1–6) correspond to the stress and strain values labeled in Fig. 4. Within each subplot (a), (b), and (c), the top panel corresponds to the experimental result, while the bottom panel corresponds to the simulation result. (a) Velocities of the particles in the pillar. The magnitude of the displacement of a particle from the current position after time interval $\Delta t = (2/15)R/v_c$ is divided by Δt to obtain the average velocity across the time interval. (b) Deviatoric strain rate J_2 for each particle. J_2 is computed by comparing the current configuration of a particle and its neighbors with the configuration after Δt, using neighbor sampling distance $R_c = 1.25D$. J_2 is measured in units of v_c/R. (c) Nonaffine displacement $D_{\min}^2$ for each particle in the pillar. The procedures for calculating $D_{\min}^2$ are discussed in the main text. See Supplemental Material for the corresponding movies [25].

of μ_g. The simulation results presented in this paper use $\mu_g = 0.2$, which is found to achieve an overall good match between the experiment and simulation.

In Fig. 4, we label several stress/strain values and calibrate the corresponding particle-level structural changes in the pillar. The experimental and simulation results are then compared side-by-side in Fig. 5. Good agreement between experiment and simulation is achieved. The small differences in the microscopic measurement can be attributed to the fact that the simulation force model does not consider the size polydispersity and shape irregularity of the granular particles, which are present in the experimental system. Other factors, such as the choice of certain model parameters (e.g., grain-grain friction coefficient), inexact match of initial conditions due to measurement uncertainty in experiment, and the use of nonzero time steps in simulation, may also contribute.

Figure 5(a) shows the mean particle velocity field in the pillar at six different stages of deformation. The mean velocity of a particle i, denoted by $v_i(t, \Delta t)$, is calculated as the average displacement magnitude of the particle from current time t to a later time $t + \Delta t$,

$$v_i(t, \Delta t) = |\mathbf{r}_i(t + \Delta t) - \mathbf{r}_i(t)|/\Delta t, \qquad (13)$$

where the value of time interval Δt is chosen to be $2/15R/v_c$ for the present purpose. $v_i(t, \Delta t)$ contains information of the absolute amount of displacement of the particle i within Δt. As shown in Fig. 5(a), the mean velocities of the particles near the moving bar are close to v_c, which is expected as the pillar is deformed quasistatically by the bar. The mean velocity of a particle in general becomes smaller as the particle is farther away from the moving bar. At the early stages of deformation, particles at the bottom part of the pillar have not moved and
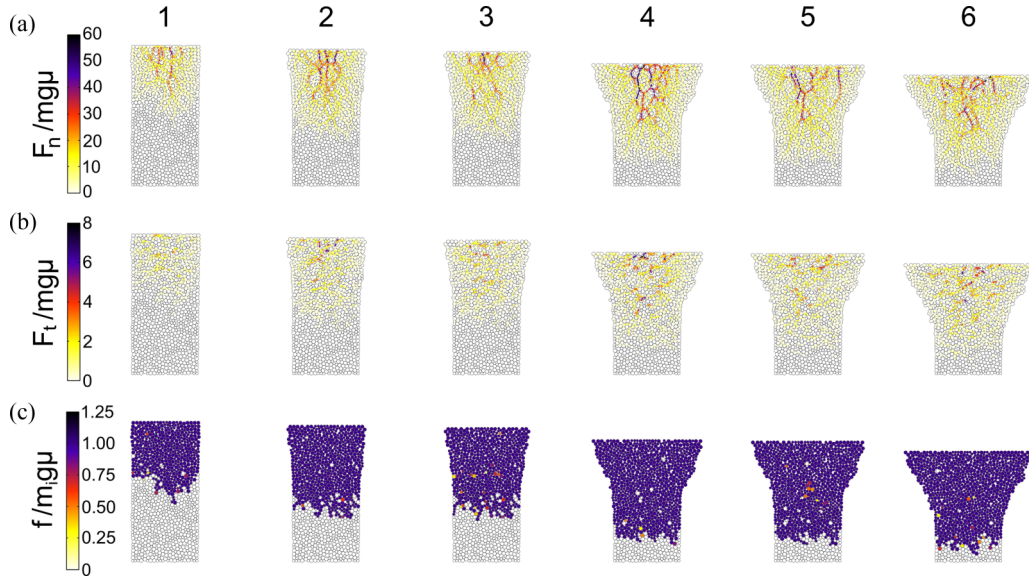
FIG. 6. (Color online) Forces in the granular pillar during deformation as obtained from simulation. The numerical labels (1–6) correspond to the deformation stages labeled in Fig. 4(b). (a) Grain-grain normal force F_n, (b) grain-grain tangential force F_t, and (c) grain-substrate friction force f. The normal and tangential forces are measured in units of $mg\mu$, which is the largest possible value of substrate-induced friction on a large grain. The substrate friction forces are measured in units of $m_i g \mu$. See Supplemental Material for the corresponding movie [25].

therefore have zero values of v. A sharp boundary between the moving and nonmoving regions of the pillar often forms along the the direction that is roughly 45° to the direction of uniaxial deformation.

In the simulations we have access to detailed information on the interparticle interactions. In Fig. 6 we plot the grain-grain normal force F_n, tangential force F_t, and substrate-induced force frictional force f on the particles at six stages of deformation corresponding to the numerical labels in Fig. 4. Comparing Fig. 6(a) with Figs. 6(b) and 6(c), we find that F_n is in general much larger than F_t, which is further larger than f, namely $F_n \gg F_t \gg f$. In particular, Fig. 6(a) shows that particles with large F_n are connected with force chains. The magnitude of forces in these force chains is higher for particles residing in the interior the pillar. This indicates that the stress in the pillar is rather inhomogeneous, with larger stresses in the interior region of the pillars than close to the surface.

We further look at the rearrangement of particles in the pillar by defining a neighbor sampling distance R_c, and calculate the affine transformation strains and nonaffine displacements of the particles with respect to their neighbors within R_c. The value of R_c is chosen to be $1.25D$, which roughly corresponds to the average first-nearest-neighbor distance of the particles in the pillar, as can be seen from the computed radial distribution functions in Fig. 2. A particle j is considered to be the neighbor of a particle i if their distance is smaller than R_c, which is illustrated in Fig. 7. The configurations of the particle i and its neighbors at a given time t and a subsequent time $t + \Delta t$ will then be used to compute the best-fit local affine transformation matrix $\mathbf{J}$ and the nonaffine displacement $D^2_{\min}$ associated with particle i, using the method introduced by Falk and Langer [9,26]. Specifically, $D^2_{\min,i}$ is obtained by calculating the best affine transformation matrix $\mathbf{J}_i$ that minimizes the

error of deformation mapping:

$$D^2_{\min,i}(t, \Delta t) = \frac{1}{N_i} \min_{\mathbf{J}_i} \sum_{j \in N_i} [\mathbf{r}_{ji}(t + \Delta t) - \mathbf{J}_i \mathbf{r}_{ji}(t)]^2, \quad (14)$$

where $\mathbf{r}_{ji}(t) = \mathbf{r}_j(t) - \mathbf{r}_i(t)$ is the distance vector between particles j and i at time t. $\mathbf{r}_{ji}(t + \Delta t)$ is the distance vector at a later time $t + \Delta t$. The summation is over the neighbors of particle i at time t, whose total number is given by N_i. The best-fit affine transformation matrix $\mathbf{J}_i(t, \Delta t)$ is usually nonsymmetric due to the presence of the rotational component. A symmetric Lagrangian strain matrix $\boldsymbol{\eta}_i$ can be calculated
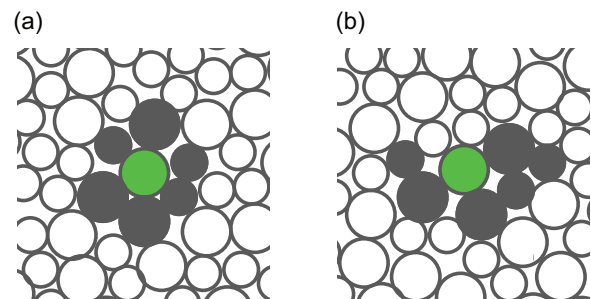

FIG. 7. (Color online) (a) Illustration of a particle (colored in green) and its neighbors (colored in black) within a cutoff distance $R_c = 1.25D$ at an initial reference configuration. (b) The same set of particles at a later stage of deformation. We seek to find the best-affine transformation matrix $\mathbf{J}$ that maps the coordinates of the particles illustrated in (a) to those in (b). This optimization procedure also gives the nonaffine displacement $D^2_{\min}$ associated with the central (green) particle, and the deviatoric strain η^s in the neighborhood, as discussed in the main text.

from $\mathbf{J}_i$ as

$$\boldsymbol{\eta}_i = \tfrac{1}{2}\big(\mathbf{J}_i^T\mathbf{J}_i - \mathbf{I}\big), \qquad (15)$$

where $\mathbf{I}$ is an identity matrix. The hydrostatic invariant is then computed from $\boldsymbol{\eta}_i$ as

$$\eta_i^m = \tfrac{1}{2}\mathrm{Tr}\boldsymbol{\eta}_i. \qquad (16)$$

The shear (deviatoric) invariant is then given by

$$\eta_i^s = \sqrt{\tfrac{1}{2}\mathrm{Tr}\big(\boldsymbol{\eta}_i - \eta_i^m\mathbf{I}\big)^2}. \qquad (17)$$

Hereafter we will refer to $\eta_i^s(t,\Delta t)$ as the deviatoric strain associated with the particle i from t to $t + \Delta t$. The deviatoric strain rate, denoted by J_2, is the normalization of $\eta_i^s(t,\Delta t)$ with respect to Δt:

$$J_2(t,\Delta t) = \eta^s(t,\Delta t)/\Delta t. \qquad (18)$$

Figures 5(b) and 5(c) show the computed deviatoric strain rate J_2 and $D_{\min}^2$ for each particle in the pillar at six different stages of deformation, where the experimental and simulation results are compared side-by-side. $J_2(t,\Delta t)$ and $D_{\min}^2(t,\Delta t)$ are computed using $\Delta t = (2/15)R/v_c$, which is the same as the value of Δt used for computing the mean velocities of the particles in Fig. 5(a). Comparing Fig. 5(b) with Fig. 5(a), it can be seen that large values of deviatoric strain rate occur at places where the gradient of mean velocity, and hence the gradient of particle displacement, is large, which is understandable as strain is a measure of displacement gradient. One can also notice from Fig. 5(b) the presence of thin shear lines in the pillars, where particles with large deviatoric strain rate reside. The width of these shear lines is about twice the diameter of the particles. These shear lines largely correspond to the moving boundary between the deformed and undeformed regions in the pillar. The presence of such shear lines will appear clearer as pillar size increases, which will be discussed in the latter part of the article.

Comparing the $D_{\min}^2$ profile in Fig. 5(c) with deviatoric strain rate J_2 in Fig. 5(b), it is clear that particles with larger values of $D_{\min}^2$ are correlated with larger values of J_2, and hence also deviatoric strain η^s [Eq. (18)]. The deviatoric strain η^s reflects the local shear component of affine deformation (shape change), while $D_{\min}^2$ measures additional particle displacement with respect to its neighbors that cannot be described by mere shape change. The positive correlation between $D_{\min}^2$ and η^s is understandable because the larger the value of η^s (which usually drives plastic deformation), the error of describing local particle rearrangement in terms of purely shape change, which is the definition of $D_{\min}^2$, will more likely to be larger.

IV. LOCAL DEVIATORIC STRAIN DRIVEN PARTICLE DIFFUSION

The positive interdependence between $D_{\min}^2$ and η^s motivates us to map out their correlation quantitatively. Starting with an initial configuration of the pillar at time t that corresponds to deformation strain $\varepsilon = v_c t/H_0$, we fix the neighbor sampling distance $R_c = 1.25D$ and calculate $\eta^s(t,\Delta t)$ and $D_{\min}^2(t,\Delta t)$ for each particle in the pillar using a logarithmic series of time intervals $\Delta t \in [2,4,8,\ldots,128]/15\,R/v_c$. This
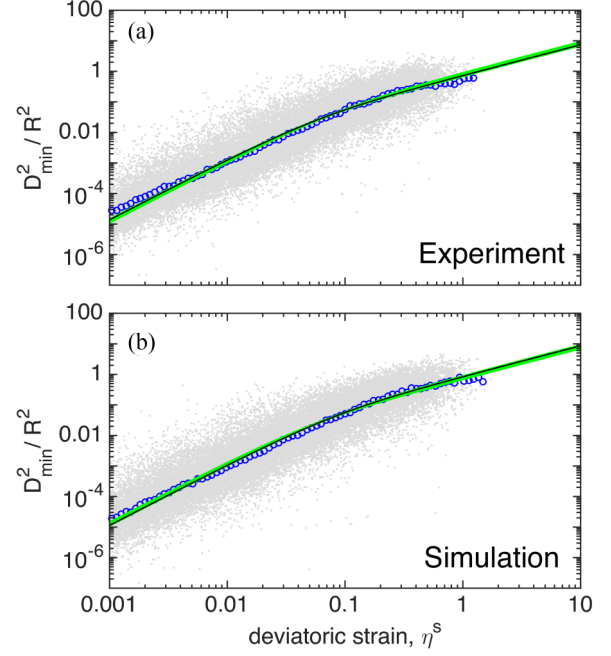

FIG. 8. (Color online) $D_{\min}^2/R^2$ vs deviatoric strain, η^s, for (a) experiment and (b) simulation. Gray points show all the data. Blue circles show the average $D_{\min}^2/R^2$ values within each of 100 η^s bins, with circle size indicative of the standard error of the mean within the bin. The blue data are fitted to an exponential crossover equation from quadratic to linear scaling [see main text and Eq. (19) for details]. The black curves in each plot show the best-fit result for the binned data, and the green region shows the full range spanned by the 95% confidence intervals of both fits.

procedure is then repeated for at least eight values of initial times t equally spaced by $\frac{2}{3}R/v_c$. We then plot all the calculated values of $D_{\min}^2(t,\Delta t)$ with respect to $\eta^s(t,\Delta t)$ on a single plot, using logarithmic axes for both $D_{\min}^2$ and η^s. The results of experiment and simulation are shown together in Fig. 8. From Fig. 8, it can be seen that while for a given specific value of η^s the possible values of $D_{\min}^2$ are scattered, the existence of statistical correlation between $D_{\min}^2$ and η^s is apparent. We find that in the range of small values of η^s, $D_{\min}^2$ scales quadratically with η^s, which gradually transits to linear scaling at larger values of η^s. This is reminiscent of the scaling relationship between the growth of mean-squared displacement (MSD) for a thermally diffusive particle and time t, which is often explained pedagogically by an unbiased random walker. Indeed, we find that, by considering $D_{\min}^2$ as MSD, and deviatoric strain η^s as time, the data in Fig. 8 can be fitted very well using the following equation that describes the exponential crossover of a thermal particle from ballistic to diffusive motion, expected for a Langevin particle with no memory [27]:

$$D_{\min}^2(\eta^s)/R^2 = 4\Theta\eta^s - 4\Theta\eta_c^s\big[1 - \exp\big(-\eta^s/\eta_c^s\big)\big], \quad (19)$$

where $D_{\min}^2$ is scaled by R^2 to render it dimensionless. Θ is the dimensionless effective diffusivity while η_c^s takes the meaning of "crossover deviatoric strain." Our fitting of the data gives the values of the parameters with 95% confidence intervals as $\Theta = 0.19 \pm 0.02$, $\eta_c^s = 0.027 \pm 0.004$

for the experiment, and $\Theta = 0.22 \pm 0.02$, $\eta_c^s = 0.038 \pm 0.005$ for the simulation.

The analogy between $D_{\min}^2$ and MSD, and between η^s and time t, may have deep implications. $D_{\min}^2$ describes the mean-squared nonaffine displacement of a particle with respect to its neighbors and can be naturally identified as an analogy to MSD. The analogy between deviatoric strain η^s and time t implies that, for the granular packings, where there is no thermal agitation and the system is deformed heterogeneously, the cumulative deviatoric strain plays the role of time and drives effective particle diffusion. Argon had originally used bubble raft deformation to illustrate the concept of shear transformation zone (STZ) [28,29], which emphasizes the affine part of localized stress-driven processes. Recently, Wang *et al.* found that cyclic mechanical loading can induce the nanocrystallization of metallic glasses well below the glass transition temperature [7,8], resulting from stress-driven accumulation of nonaffine displacement of the atoms in the sample. The concept of shear diffusion transformation zones (SDTZs) was proposed by the authors to explain the experimental results and to emphasize the diffusive character of STZs. Our results lend support to the concept of SDTZ by showing that, even in amorphous granular packings, where there is no thermally driven diffusion at all, if the accumulated local deviatoric strain is large enough (above a few percent strain), the nonaffine displacement of a particle with respect to its neighbors crosses over to the diffusive limit. This suggests that SDTZ may be a key concept for a broad range of amorphous solids.

The analogy between local cumulative shear transformation strain in athermal amorphous solids and time in thermal systems for particle diffusion may be rationalized by a "space-time equivalence" argument, as follows. A finite temperature $k_B T$ means temporally random momentum fluctuations, for crystals and noncrystals alike. Even in crystals, such random momentum fluctuations (due to collision of multiple phonons) can drive the random walker behavior of a particle, if these temporal fluctuations can be significant compared to the potential energy barrier. But in amorphous solids without spontaneous temporal fluctuations, there will be nonetheless still another source of randomness, which is the local spatial structure and structural response of the amorphous solid. This is indeed what motivated the "heterogeneously randomized STZ model" [30,31]. In other words, even if two "Eshelby inclusions" at different locations of an amorphous solid transform by exactly the same transformation strain η, one reasonably would still expect drastically different internal particle arrangements and rearrangements inside these zones. This ultimately is because the local strain η is just a coarse-graining variable, that represents a key aspect of the structural transformations of a kinetically frozen random cluster, but not all of its structural information. (This may not be true in simple crystals, where η may entirely capture the entire structure.) Such structural mutations beyond transformation strain are reflected in $D_{\min}^2$. The fact that $D_{\min}^2$ will accumulate linearly with strain at steady state means the structural mutations from generation to generation [30,31] are largely nonrepeating and essentially unpredictable, if starting from a spatially random configuration at the beginning, even when the stress condition driving these transformations remains largely

the same. Our experiment and simulation on compressing amorphous granular pillars can thus be seen as a "spatial random number generator" with the initial configuration as the "random number seed," in contrast to more well-known "temporal random number generator" algorithms; but both types of algorithms tend to give long-term uncorrelated increments for the random walker.

V. SIMULATION OF SIZE-DEPENDENT PILLAR DEFORMATION

Having achieved good agreement between experiment and simulation for the $N = 1000$ pillar, we now take advantage of the fact that our simulation can treat much larger systems than experiment to study the size-dependent deformation behavior of the granular pillars by simulation. (The system size that can be accessed in experiment is limited by the physical dimensions of the apparatus.) Three large-sized pillars, denoted by $N = 4000$, $N = 16\,000$, and $N = 64\,000$, are deformed by the top bar moving at the same deformation speed v_c. The aspect ratio of the pillars (2 to 1) is fixed to be the same value of the $N = 1000$ pillar. As the initial packing density of the particles in the pillar is also the same, the initial width of the pillars W_0 scales as $\sqrt{N}$.

We find that the macroscopic shape evolution of the different-sized pillars is self-similar during deformation. At the same values of deformation strain $\varepsilon = \Delta H / H_0$, we extract the boundaries of the pillars, rescale them by the respective initial pillar width W_0, and plot them together in Fig. 9. The rescaled boundaries of the pillars are nearly identical to each other. This implies that the width at the top of a pillar, W, divided by the original width, W_0, does not depend strongly on the pillar size and is therefore approximately only a function of strain ε; i.e, $W/W_0 = \chi(\varepsilon)$, where the scaling function χ does not depend on the pillar width W_0.

We also find that the average flow stress of the pillars increases linearly with the initial pillar width W_0, as shown in Figs. 10(a) and 10(b). Mathematically, this can be expressed as $\langle \sigma \rangle \propto W_0$, where we define $\langle \sigma \rangle$ to be the average flow stress for strain ε between 0.05 and 0.2. This scaling behavior for the flow stress indicates that, for the 2D disordered granular pillars, the behavior of "smaller is weaker" is exhibited. This is quite different from the deformation of freestanding metallic glass pillars, where "smaller is stronger" is the general trend [32,33].

To understand the surprising size dependence of flow stress, we first look at the stress distribution in the pillars. In Fig. 5 we have shown that the grains in the interior region of the pillar experience larger interparticle contact forces, resulting in larger local stress in the interior region of the pillar. The rate of increase for local stress as a function of distance to the lateral edges of the pillars is found to be very close for different-sized pillars. Such stress nonuniformity should also be reflected in the local contact pressure between the moving bar and the pillar. Indeed, we find that the contact pressure is also spatially rather nonuniform. Figure 10(c) shows that the local contact pressure increases almost linearly from near zero at the edge of the pillar to saturated values around the center of contact interface. The maximum values of local contact pressure scale roughly linearly with pillar width, consistent with the linear scaling of pillar flow stress.
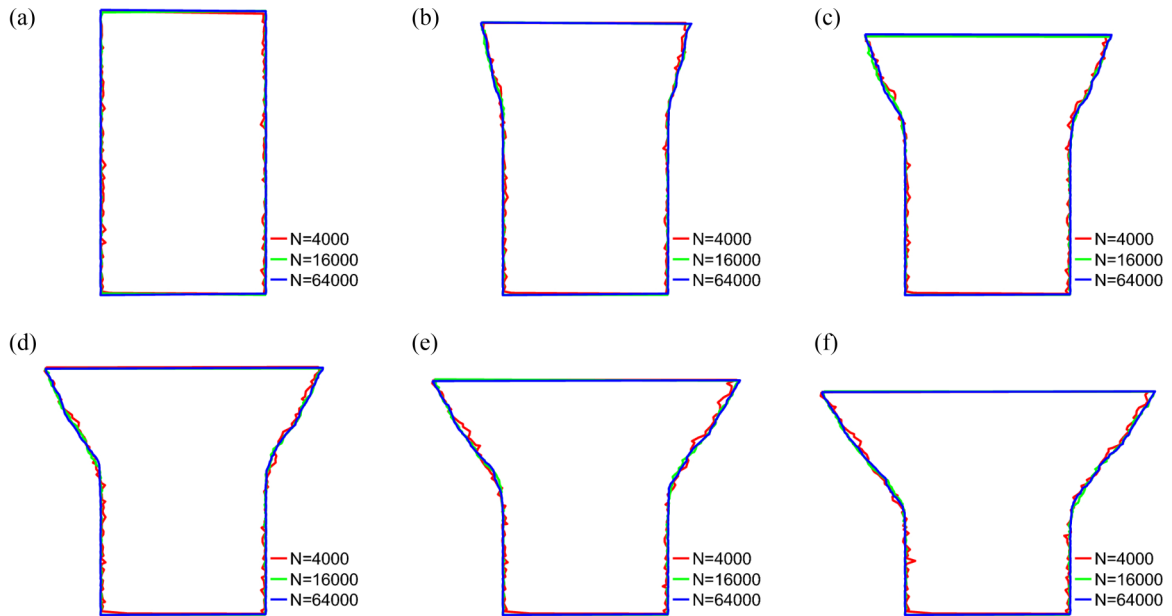
FIG. 9. (Color online) Self-similar evolution of pillar shapes during deformation of different-sized pillars. The boundaries of three pillars ($N = 4000$, $N = 16\,000$, and $N = 64\,000$) are rescaled and plotted together at the same strain value.
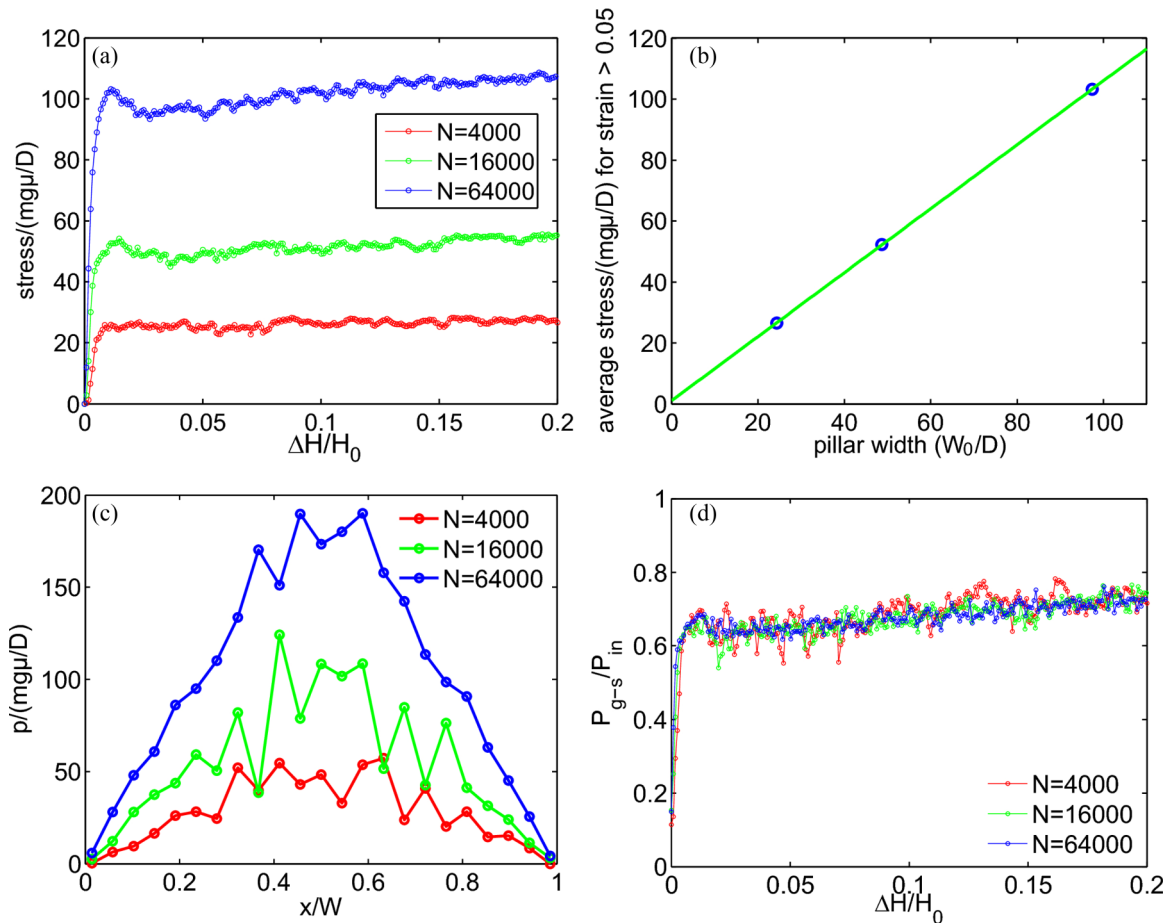

FIG. 10. (Color online) Size-dependent flow stress and dissipation of input power. (a) Stress-strain curves for different-sized pillars. (b) Linear scaling of average flow stress with respect to pillar width W_0. The average flow stress is computed for the range of strain between 0.05 and 0.2. (c) Local contact pressure p between the moving bar and the pillars as a function of position x along the contact interface, computed for different-sized pillars at the same macroscopic strain value in the plastic flow regime. The position x is scaled by the width of the pillar W at the contact interface. (d) Fraction of input power dissipated by the grain-substrate translational friction as a function of deformation strain for different-sized pillars.
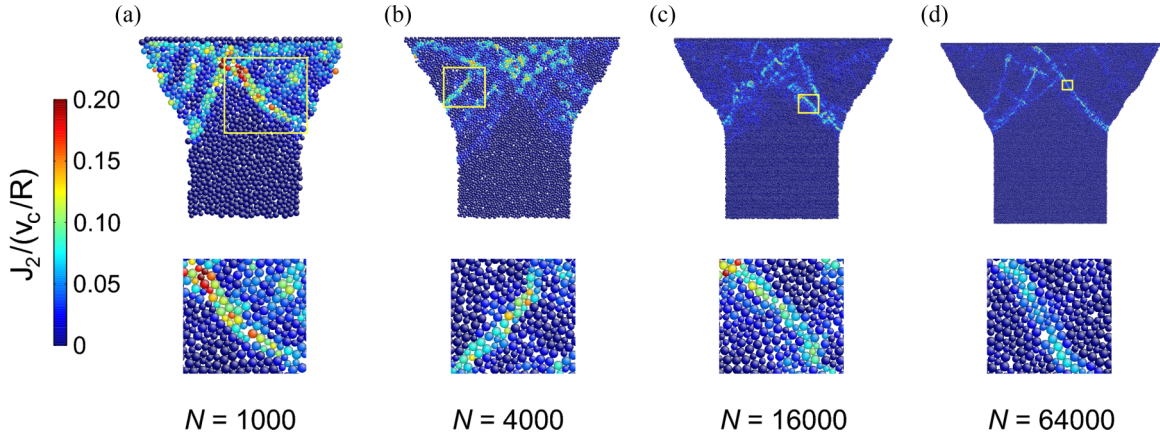
FIG. 11. (Color online) Deviatoric strain rate J_2 associated with each particle and zoom-in views of the transient shear lines in different-sized pillars. Four different-sized pillars are compared with each other, which contain 1000, 4000, 16 000, 64 000 grains (from left to right). The regions in the pillars for zoom-in views are indicated by squares. For each pillar, the two configurations of pillars used for J_2 calculation are separated by time difference $\Delta t = 8/15 \ R/v_c$. See Supplemental Material for the corresponding movie [25].

Since the pillars are deformed quasistatically, most of the deformation work on the pillars will be dissipated during plastic flow. The flow stress is therefore closely related to the dissipation of energy in the systems. We hence study how the energy dissipation in the pillars changes with pillar size. As the granular particles in the pillars stand on a substrate, two major mechanisms of energy dissipation during plastic flow can be identified: grain-substrate friction and grain-grain friction. The total external power input by the moving bar into the pillar, denoted by P_{in}, can be calculated as

$$P_{in} = F_{bar} v_c = \sigma W v_c. \tag{20}$$

We have shown that, compared at the same deformation strain ε, both the flow stress σ and pillar width W are proportional to the initial pillar width W_0. Hence, the input power by the external force scales quadratically with W_0, namely $P_{in} \propto W_0^2$. As most of the input power will be dissipated in the plastic flow regime, the dissipated power should also scale with W_0^2.

To study how the dissipated input power is distributed between the substrate-induced friction and grain-grain friction, we compute the fraction of input power dissipated by the grain-substrate frictional force and study its size dependence. The power dissipation by grain-substrate friction includes contributions from both the translational sliding and rotational motion of the particles. We find that the power dissipation due to rotational motion is more than an order of magnitude smaller than the dissipation by translational sliding. The contribution from the rotational motion of the particles is therefore not explicitly included in the calculation below. The amount of power dissipated by the grain-substrate (translational) friction force, denoted by $P_{g\text{-}s}$, can be calculated as

$$P_{g\text{-}s} = \sum_i m_i g \mu v_i, \tag{21}$$

where the particle mean velocity v_i has the same definition as in Eq. (13), namely the average displacement of the particle i within a small time interval Δt. The fraction of power dissipated by the substrate-induced friction, denoted by κ, is then given by $\kappa \equiv P_{g\text{-}s}/P_{in}$. We calculate the values of κ for different-sized pillars and plot them as a function of

deformation strain in Fig. 10(d). The result indicates that κ is statistically independent of pillar size. This allows us to conclude that the amount of input power dissipated by grain-substrate friction, $P_{g\text{-}s} = \kappa P_{in}$, also scales quadratically with pillar size W_0, and hence scales linearly with the number of particles in the pillar N. This effectively means that the number of particles participating in the plastic flow scales linearly with the total number of particles in the pillar, which is consistent with the self-similar shape evolution of the pillars.

The calculated values of κ in Fig. 10(d) indicate that the majority of deformation work is dissipated by the friction between the particles in the pillar and the substrate. Substrate friction therefore must play an important role in the linear increase of flow stress with respect to pillar width and the self-similar evolution of pillar shape, which have been shown to be consistent with each other. The granular pillars in our study are not truly two-dimensional due to the presence of grain-substrate friction. This setup is however necessary for stable plastic flow of the uniaxially deformed granular pillars without cohesive interparticle interaction. Without the grain-substrate friction, the deformation behavior of the granular pillars are expected to be quite different, and the size-dependent deformation behavior observed in this study (i.e., "smaller is weaker") may no longer hold.

If the macroscopic shape evolution of the pillars in our systems is self-similar, then how does the local yielding behavior vary with pillar size? We characterize the deformation-induced local structural change of the pillar by computing the deviatoric strain rate J_2 associated with each particle between two stages of deformation, using the same methodology described earlier in the article. We find that, within a small amount of pillar strain, particles with large values of J_2 organize into thin shear lines, which becomes more evident as pillar size increases, as shown in Fig. 11. These shear lines orient along the direction about 45° to the direction of uniaxial compression. Clearly, such shear lines form along the direction of maximum shear stress. The sharpest shear lines appear predominantly at the moving boundary between the deformed and undeformed region in the pillars, as mentioned in the combined experimental and simulation study of small-sized

pillars in Sec. III. A close-up view of these shear lines in Fig. 11 indicates that the width of the shear lines does not change as pillar size increases, maintaining a value about twice the diameter of a grain. We emphasize that these shear lines are transient in time. As deformation goes on, new shear lines will form elsewhere in the pillar, while the particles in the shear lines formed earlier may not accumulate a significant amount of shear strain continuously. Evidence of such transient shear bands in granular materials was previously reported in the discrete-element simulations by Aharonov and Sparts [34] and Kuhn [35,36]. Maloney and Lemaître [37] and Tanguy *et al.* [38] observed transient lines of slip in their athermal, quasistatic simulation of 2D glasses of frictionless particles, and explained their formation in terms of elastic coupling and cascading of shear transformation zones. The results of our combined experiment (Fig. 5) and simulation of uniaxial, quasistatic deformation of 2D granular pillars clearly demonstrate the existence of such transient shear lines, which carry localized deformation in the granular pillars.

The size-independent width of the transient shear lines is surprising since the overall macroscopic shape of the pillar is self-similar in systems of different sizes. Despite the self-similarity at the macroscopic scale, the system is not self-similar in how it yields at the microscopic scale. Since the slip lines are independent of system size, there must be more of them in larger systems, which is indeed observed in our simulation. Why the system chooses to be self-similar at the macroscopic scale but not at the microscopic scale is an interesting point for future study.

VI. CONCLUDING REMARKS

We have carried out combined experiments and simulations of the quasistatic, uniaxial deformation of 2D amorphous granular pillars on a substrate. The simulation model developed in

this article achieves good quantitative match to the experiment. In particular, we find that, for the granular packings, the nonaffine displacements of the particles exhibit exponential crossover from ballistic to diffusion-like growth behavior with respect to local deviatoric strains. This result is a generalization to inhomogeneous loading of earlier observations of stress-driven diffusion of particles in simulated 2D molecular glasses under simple shear or pure shear in the thermal, quasistatic limit [6,38–42]. Because in our study the "time" variable for diffusion, the best-fit deviatoric strain in a neighborhood, is a local measure of deformation and shear transformation, we expect that the nonaffine displacement should cross over from ballistic to diffusive behavior in amorphous solids under any loading conditions.

In metallic glass pillars, the apparent strength of the pillar and strain localization behavior depends on pillar diameter, manifesting so-called "size-dependent plasticity" behavior [31]. Often, "smaller is stronger" holds for metallic glasses [32,33]. We have shown that for 2D granular pillars on a substrate, the frictional interaction between the granular particles and the substrate leads to the opposite size-dependent response, namely "smaller is weaker."

Finally, our combined experiment and simulation study clearly demonstrates that transient lines of slip form in quasistatically deformed amorphous granular pillars under uniaxial loading conditions. These system-spanning shear lines carry localized shear transformations in 2D granular pillars, and their width shows no size dependence. Altogether, these results could have important implications for the plasticity and internal structural evolution of amorphous solids.

ACKNOWLEDGMENTS

[1] A. L. Greer, Y. Cheng, and E. Ma, Mater. Sci. Eng., R **74**, 71 (2013).

[2] M. L. Falk and J. S. Langer, Annu. Rev. Condens. Matter Phys. **2**, 353 (2011).

[3] H. M. Jaeger, S. R. Nagel, and R. P. Behringer, Rev. Mod. Phys. **68**, 1259 (1996).

[4] P. de Gennes, Rev. Mod. Phys. **71**, S374 (1999).

[5] E. D. Cubuk, S. S. Schoenholz, J. M. Rieser, B. D. Malone, J. Rottler, D. J. Durian, E. Kaxiras, and A. J. Liu, Phys. Rev. Lett. **114**, 108001 (2015).

[6] I. K. Ono, C. S. O'Hern, D. J. Durian, S. A. Langer, A. J. Liu, and S. R. Nagel, Phys. Rev. Lett. **89**, 095703 (2002).

[7] C.-C. Wang, Y.-W. Mao, Z.-W. Shan, M. Dao, J. Li, J. Sun, E. Ma, and S. Suresh, Proc. Natl. Acad. Sci. USA **110**, 19725 (2013).

[8] Y.-W. Mao, J. Li, Y.-C. Lo, X.-F. Qian, and E. Ma, Phys. Rev. B **91**, 214103 (2015).

[9] M. L. Falk and J. S. Langer, Phys. Rev. E **57**, 7192 (1998).

[10] J. M. Rieser *et al.* (unpublished).

[11] J. M. Rieser, P. E. Arratia, A. G. Yodh, J. P. Gollub, and D. J. Durian, Langmuir **31**, 2421 (2015).

[12] C. S. O'Hern, L. E. Silbert, A. J. Liu, and S. R. Nagel, Phys. Rev. E **68**, 011306 (2003).

[13] K. L. Johnson, *Contact Mechanics* (Cambridge University Press, Cambridge, 1985).

[14] L. E. Silbert, D. Ertaş, G. S. Grest, T. C. Halsey, D. Levine, and S. J. Plimpton, Phys. Rev. E **64**, 051302 (2001).

[15] P. A. Cundall and O. D. L. Strack, Geotechnique **29**, 47 (1979).

[16] L. E. Silbert, G. S. Grest, and J. W. Landry, Phys. Rev. E **66**, 061303 (2002).

[17] J. W. Landry, G. S. Grest, L. E. Silbert, and S. J. Plimpton, Phys. Rev. E **67**, 041303 (2003).

[18] R. Brewster, G. S. Grest, J. W. Landry, and A. J. Levine, Phys. Rev. E **72**, 061301 (2005).

[19] H. P. Zhang and H. A. Makse, Phys. Rev. E **72**, 011301 (2005).

[20] C. H. Rycroft, G. S. Grest, J. W. Landry, and M. Z. Bazant, Phys. Rev. E **74**, 021306 (2006).

[21] C. H. Rycroft, M. Z. Bazant, G. S. Grest, and J. W. Landry, Phys. Rev. E **73**, 051306 (2006).

[22] K. Kamrin, C. H. Rycroft, and M. Z. Bazant, Model. Simul. Mater. Sci. Eng. **15**, S449 (2007).

[23] C. H. Rycroft, A. V. Orpe, and A. Kudrolli, Phys. Rev. E **80**, 031305 (2009).

[24] C. H. Rycroft, K. Kamrin, and M. Z. Bazant, J. Mech. Phys. Solids **57**, 828 (2009).

[25] See Supplemental Material at http://link.aps.org/supplemental/10.1103/PhysRevE.91.062212 for movies of the quantities displayed in Figs. 5, 6, and 11.

[26] F. Shimizu, S. Ogata, and J. Li, Mater. Trans. **48**, 2923 (2007).

[27] P. M. Chaikin and T. C. Lubensky, *Principles of Condensed Matter Physics* (Cambridge University Press, Cambridge, 2000).

[28] A. S. Argon and H. Y. Kuo, Mater. Sci. Eng. **39**, 101 (1979).

[29] A. S. Argon, Acta Metall. **27**, 47 (1979).

[30] P. Zhao, J. Li, and Y. Wang, Int. J. Plasticity **40**, 1 (2013).

[31] P. Zhao, J. Li, and Y. Wang, Acta Mater. **73**, 149 (2014).

[32] C.-C. Wang, J. Ding, Y.-Q. Cheng, J.-C. Wan, L. Tian, J. Sun, Z.-W. Shan, J. Li, and E. Ma, Acta Mater. **60**, 5370 (2012).

[33] D. Jang and J. R. Greer, Nat. Mater. **9**, 215 (2010).

[34] E. Aharonov and D. Sparks, Phys. Rev. E **65**, 051302 (2002).

[35] M. R. Kuhn, Mech. Mater. **31**, 407 (1999).

[36] M. R. Kuhn, Granul. Matter **4**, 155 (2003).

[37] C. E. Maloney and A. Lemaître, Phys. Rev. E **74**, 016118 (2006).

[38] A. Tanguy, F. Leonforte, and J.-L. Barrat, Eur. Phys. J. E **20**, 355 (2006).

[39] A. Lemaître and C. Caroli, Phys. Rev. E **76**, 036104 (2007).

[40] C. E. Maloney and M. O. Robbins, J. Phys.: Condens. Matter **20**, 244128 (2008).

[41] A. Lemaître and C. Caroli, Phys. Rev. Lett. **103**, 065501 (2009).

[42] K. Martens, L. Bocquet, and J.-L. Barrat, Phys. Rev. Lett. **106**, 156001 (2011).